PAPER

Engineering a covalently linked NH₂−TiN@PCN-222-Co single atom-based photocatalyst for solar-driven CO₂-to-CO conversion†

Minh-Khoa Duong,[a] Toan-Anh Quach,[a] Van-Duc Nguyen, [b] [a] Sakar Mohan [b] [b] and Trong-On Do [b] *[a]

In this study, we report the synthesis of NH_2-functionalized titanium nitride (TiN) nanoparticles (NPs) incorporated into single cobalt atom-integrated PCN-222 (denoted as TiN@PCN(Co)-x, where x represents the wt% of TiN) *via* a solvothermal approach. The amino-functionalized TiN NPs establish strong chemical bonding with PCN-222-Co, facilitating charge transport from the photosensitizer $[Ru(bpy)_3]^{2+}$ to PCN-222-Co and thereby significantly enhancing photocatalytic CO_2 reduction. Notably, the photosensitizer $[Ru(bpy)_3]^{2+}$ plays a crucial role as a primary electron donor, ensuring sustained charge separation and an extended electron lifetime within the TiN@PCN(Co) system. Under optimized reaction conditions, TiN@PCN(Co) with 5 wt% TiN achieves a remarkable CO production rate of 627.42 μmol g^{-1} h^{-1} after 4 h of solar light irradiation, demonstrating the synergistic effects of TiN functionalization and photosensitizer-mediated charge transfer in enhancing photocatalytic performance. These studies provide valuable insights into the design of MOF-based hybrid single atom-based photocatalysts for efficient CO_2 reduction and sustainable solar fuel production.

1. Introduction

For decades, the continuous rise of CO_2 concentration in the atmosphere has been one of the most pressing challenges for scientists worldwide. As a primary greenhouse gas, CO_2 drives climate change, threatening both natural ecosystems and human societies. The urgent need to address this crisis has spurred intensive research into CO_2 mitigation strategies, with particular focus on converting this greenhouse gas into valuable chemical products. These strategies simultaneously address environmental concerns while creating opportunities for the development of sustainable and profitable industries. Numerous efforts have been made to improve the efficiency and selectivity of CO_2 conversion reactions such as electrochemical,[1] thermochemical,[2] biochemical,[3] and photocatalytic conversion.[4–6] Among various methods for CO_2 utilization, photocatalysis has emerged as a promising method due to its low cost and environmental friendliness.

Inspired by natural photosynthesis, photocatalytic CO_2 conversion utilizes a light-harvesting catalyst to transform solar energy into chemical energy. Over the years, numerous materials have been developed as photocatalysts for CO_2 photoreduction, including metal oxides[7,8] (*i.e.*, TiO_2, ZnO, and SnO_2) and carbon-based materials[9,10] (graphene and graphitic carbon nitride). However, these traditional semiconductors have their own shortcomings, including low CO_2 adsorption capacity, wide band gap energy, and fast charge recombination. As a result, the current research tends to focus on more complex and tailored materials. In this direction, metal–organic frameworks (MOFs) have emerged as promising candidates for photocatalysts with advantageous physical and chemical properties owing to their large surface areas, well-ordered porous structures, and tunable organic linkers and metal clusters.[11–14]

In recent years, MOF-based photocatalysts such as MOF-5, UiO-66, MIL-125, PCN-222, *etc.*, exhibiting semiconductor-like behaviors, were rapidly developed and employed as potential photocatalysts. Among these MOF materials, PCN-222 shows unique characteristics suitable for photocatalytic CO_2 reduction. PCN-222 is a microporous crystalline material, which is based on the coordination connection of $Zr_6(O)_4(OH)_4$ nodes and tetrakis(4-carboxyphenyl)-porphyrin (H_2TCPP) linkers. This H_2TCPP linker can confine an isolated metal atom and act as an active site in a ring composed of four pyrrole rings, thereby promoting the chemical reducing ability. Its high surface area results in enhanced CO_2 adsorption capacity, abundant active sites, excellent mass transfer capacity and strong visible light absorption.

[a] Department of Chemical Engineering, Laval University, 1065 Avenue de la Médecine, Quebec, QC G1V0A6, Canada. E-mail: Trong-On.Do@gch.ulaval.ca

[b] Centre for Nano and Material Sciences, Jain (Deemed-to-be University), Jain Global Campus, Kanakapura road, Bangalore 562112, Karnataka, India

† Electronic supplementary information (ESI) available. See DOI: https://doi.org/10.1039/d5tc01575h

Due to these characteristics, PCN-222 has been widely investigated as a photocatalyst for various applications, including CO_2 conversion,[15] hydrogen generation,[16] and water treatment.[17] On the other hand, TiN nanoparticles are considered as an alternative to plasmonic noble metals due to their thermal/chemical stability and low cost. Notably, TiN exhibits localized surface plasmon resonance (LSPR), which can improve the visible light absorption and injection of active hot charge carriers into semiconductors.[18] The Ohmic junction at the TiN/semiconductor interface allows charge carriers to migrate easily in both directions without significant resistance.

In this context, herein, we report a facile synthesis of a TiN/PCN-222-Co composite with a strong chemical bonding between NH_2-functionalized TiN and single cobalt atom incorporated PCN-222 *via* a solvothermal method. The integration of TiN nanoparticles in PCN-222 enhances the light harvesting capacity, while the Co single atoms on PCN-222 promote CO_2 reduction. Notably, the functionalization of titanium nitride (TiN) nanoparticles with amino groups plays a critical role in enhancing the interfacial interaction with the PCN-222(Co) framework. Specifically, the $-NH_2$ groups on the surface of TiN can form strong covalent bonds with the carboxyl groups of the Co-porphyrin linker (Co-TCPP) in PCN-222(Co). The presence of chemical bonding between these two components not only ensures stable integration of TiN into the MOF structure but also facilitates efficient charge transfer across the interface and suppresses charge recombination, thereby enhancing the overall photocatalytic performance of the system.

2. Experimental section

2.1. Chemicals

Titanium nitride 80 nm (TiN, 99.2+%, cubic) was purchased from US Research Nanomaterials, Inc. Cobalt(II) chloride hexahydrate ($CoCl_2 \cdot 6H_2O$), methyl *p*-formylbenzoate (98%), propionic acid (99%), and benzoic acid (99%) were purchased from Oakwood Chemical. (3-Aminopropyl)triethoxysilane (APTES, 98%) was purchased from Alfa Aesar. Tris(2,2′-bipyridyl)dichlororuthenium(II) hexahydrate ([Ru(bpy)$_3$]Cl$_2 \cdot 6H_2O$, 99.5%), zirconium(IV) chloride (ZrCl$_4$, anhydrous, 99.5%), *N*,*N*-dimethylformamide (DMF, 99%), triethanolamine (TEOA), and acetonitrile (MeCN, anhydrous, 99.8%) were purchased from Sigma-Aldrich.

2.2. Materials synthesis

2.2.1. Synthesis of NH$_2$-functionalized titanium nitride nanoparticles (TiN–NH$_2$). The synthesis of NH$_2$-functionalized TiN was conducted following a previously reported procedure.[18] Firstly, 700 mg of titanium nitride was introduced into a mixture of HCl/H$_2$O$_2$/H$_2$O with a volume ratio of 1:1:5 and stirred for 15 min. The solid was collected by centrifugation and washed with 50 mL of ethanol 2 times. Then the solid was redispersed in 100 mL of EtOH under sonication for 1 h. A mixture of ATPES/EtOH (v:v = 1:10) was added dropwise to the pretreated TiN solution and kept at room temperature for 18 h under stirring. The NH$_2$-functionalized TiN NPs were collected

by centrifugation and washed with 100 mL of EtOH. The final product was obtained after drying in an oven at 70 °C for 5 h.

2.2.2. Synthesis of TCPP-Co. The porphyrin-based TCPP with a single metal atom attached to the center of pyrrole rings was prepared according to the report by Feng *et al.* with some modification.[19] The synthesis process consists of three steps as given below.

2.2.2.1. 5,10,15,20-Tetrakis(4-methoxylcarbonylphenyl)porphyrin (TPPCOOMe). Firstly, 6.9 g of methyl *p*-formylbenzoate and 3 g of pyrrole were added into a 250 mL flask. Then, 100 mL of propionic acid was introduced into the mixture and stirred for 30 min. After that, the mixture was refluxed at 150 °C for 12 h in the dark and left to cool down to room temperature. The obtained solution was vacuum filtered and washed with large amounts of EtOH, ethyl acetate and THF. A purple crystalline solid was obtained after drying in an oven at 70 °C for 12 h.

2.2.2.2. 5,10,15,20-Tetrakis(4-methoxylcarbonylphenyl)porphyrin-Co (TPPCOOMe-Co). A mixed solution of 0.884 g of TPPCOOMe, 3.1 g of CoCl$_2 \cdot 6H_2O$ and 100 mL of DMF was added into a 250 mL flask and stirred for 30 min. Then the mixture was refluxed at 150 °C for 6 h and left to cool down to room temperature. After that, 150 mL of H$_2$O was added to the obtained solution, resulting in a dark purple precipitate. The resulting precipitate was collected by centrifugation and washed twice with H$_2$O. The obtained solid was then dissolved in chloroform (CHCl$_3$), followed by washing three times with water. During the extraction, the organic layer was dried over anhydrous magnesium sulfate and evaporated by using a rotary evaporator, yielding purple-red crystals.

2.2.2.3. Tetrakis(4-carboxyphenyl)porphyrin-Co(II) (TCPP-Co). 0.75 g of the obtained ester (TPPCOOMe-Co) was stirred in a mixture of 25 mL of THF and 25 mL of MeOH. Then, a solution of 2.4 g of NaOH in 25 mL of H$_2$O was added to the mixture. The resultant solution was refluxed at 90 °C for 12 h and left to cool down to room temperature. The THF and MeOH in the obtained solution were removed by using a rotary evaporator. Next, 150 mL of water was added to the remaining water phase and the mixture was heated to completely dissolve the solid phase. The homogeneous solution was acidified with 1 M HCl until the pH reached around 3.0. The purple solid was collected by centrifugation, washed with water, and dried overnight at 60 °C, which is designated as TCPP-Co.

2.2.3. Synthesis of the TiN@PCN-222-Co composite. The synthesis of the chemically bonded nanocomposite is shown in the Fig. 1. Firstly, 150 mg of the synthesized TCPP-Co and a desired amount of TiN–NH$_2$ were introduced into 100 mL of DMF and stirred for 24 h. Next, 150 mg of ZrCl$_4$, 3.75 g of benzoic acid, and 3 mL of water were added to the TCPP–TiN mixture. The mixture after stirring for 15 min was transferred to a 150 mL Teflon-lined autoclave. The autoclave was then sealed and heated at 120 °C for 18 h. Then, the resulting solid was collected by centrifugation and washed with ethanol three times. The collected solid was dried in a vacuum oven overnight, and thus the TiN incorporated PCN-single-atom Co system was obtained as a dark red-brown solid. This series of
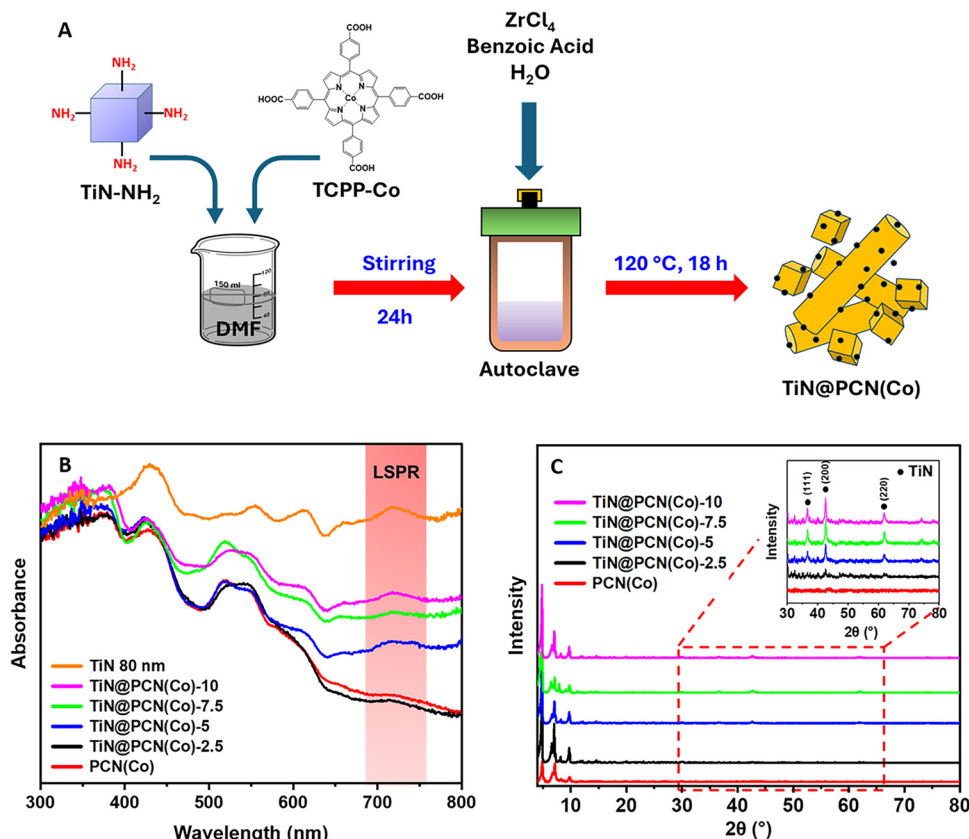
16290 | *J. Mater. Chem. C*, 2025, **13**, 16289–16301

This journal is © The Royal Society of Chemistry 2025

Fig. 1 (A) The illustration of the synthesis procedure of TiN@PCN(Co) nanocomposites; (B) UV-visible absorption spectra of bare TiN, PCN(Co), and TiN@PCN(Co) materials; (C) XRD spectra of PCN(Co) and TiN–PCN(Co) materials.

samples is denoted as TiN@PCN(Co)-x, where x is the weight percent of TiN (x = 2.5, 5, 7.5, and 10).

2.3. Photocatalytic experiments

For the photoreduction of CO_2, the photocatalyst was transferred to a 40 mL quartz test tube and dispersed in a reaction medium containing $MeCN : H_2O : TEOA$ (3 : 1 : 1 vol) with a total volume of 10 mL along with 10 mg of $[Ru(bpy)_3]Cl_2 \cdot 6H_2O$ in a 40 mL glass vial. Before solar light irradiation, CO_2 gas (99.9%, Praxair) was bubbled into the reaction solution in the dark for 10 min. After that, the quartz tube was sealed with a rubber septum, followed by solar light irradiation with ABET SN103 Model 11002 SunLite Solar Simulators (150 W Xe lamp, AM 1.5G, 100 mW cm^{-2}). The product of the photocatalytic CO_2 reduction was sampled using a gastight syringe and analyzed using a GC equipped with a TCD-FID detector and a Carboxen™ 1010 PLOT column. The major CO_2-reduction product was CO with a small amount of H_2.

2.4. Characterization

Fourier transform infrared (FT-IR) spectra were recorded using KBr pellets on a PerkinElmer Spectrum 3™ FT-IR spectrometer. The crystalline phase of the developed materials was analyzed using X-ray diffraction (XRD) on a Bruker SMART APEX II X-ray diffractometer equipped with a Cu Kα radiation source. The optical properties were investigated by UV-vis absorption (Cary 300 Bio UV-vis spectrophotometer) and photoluminescence

(PL) spectroscopy. The steady-state PL and time-resolved PL measurements were conducted on a PTI QuantaMaster 8000. The PL spectra were measured at room temperature using an excitation wavelength of 600 nm. The time-resolved fluorescence emission spectra were obtained at 500 nm under excitation using a 369 nm light source at room temperature with time-correlated single-photon counting.

The photoelectrochemical measurements were performed in a three-electrode system (Autolab PGSTAT204) irradiated with simulated solar light (150 W Xe lamp). A Na_2SO_4 (0.25 M) solution was used as an electrolyte. The counter and reference electrodes were a Pt wire electrode and an Ag/AgCl cell, respectively. The working electrode was prepared by dispersing 20 mg of the photocatalyst in 5 mL of ethanol, which was then coated onto an FTO glass (2.5 cm × 5 cm) by a spin-coating technique. During the analysis, the photocurrent was recorded by a series of switching on/off light irradiation cycles every 10 s for 250 s. The electrochemical impedance spectra (EIS) were also recorded in the frequency range from 0.1 MHz to 0.1 Hz in the dark. The Mott–Schottky analysis was performed in the potential range of −1.0 to 1.5 V at frequencies of 2500, 1000, and 500 Hz.

3. Results and discussion

As reported, the NH_2-functionalized titanium nitride (TiN) nanoparticles (NPs) were incorporated into single cobalt

This journal is © The Royal Society of Chemistry 2025

J. Mater. Chem. C, 2025, **13**, 16289–16301 | **16291**

atom-integrated PCN-222 (denoted as TiN@PCN(Co)-x, where x represents the wt% of TiN such as 2.5, 5, 7.5, and 10) via strong chemical bonding between the NH$_2$-group and the carboxyl (–COOH) group in PCN-222-Co (Fig. 1A). In this system, TiN NPs exhibit negligible plasmon resonance (PR) effects, indicating that their role in photocatalysis stems primarily from interfacial charge transfer rather than plasmonic enhancement. Comprehensive structural and spectroscopic characterization tests reveal that the enhanced photocatalytic activity originates from the formation of intimate bonding between TiN NPs and PCN-222-Co, which modifies the band gap and promotes efficient charge migration while suppressing charge recombination.

The optical properties of the synthesized materials were analyzed using UV-visible spectroscopy. Fig. 1B presents the UV-visible absorption spectra of TiN@PCN(Co) composites with various loadings of NH$_2$-functionalized TiN nanoparticles (80 nm) in the wavelength range from 300 to 800 nm. The bare PCN(Co) and its composites exhibit the characteristic Soret band edge at 422 nm and Q band edges between 519 and 660 nm. These Q bands show decreased intensity and are less defined compared to those of non-metalated PCN-222, indicating successful incorporation of cobalt ions into the porphyrin ring[20] (Fig. S1, ESI†). Upon the TiN incorporation into PCN-222, all composites show a LSPR characteristic peak at 740 nm.[21] The presence of this peak in all composites, except the bare PCN(Co), suggests effective integration of plasmonic TiN nanoparticles onto the PCN-222 structure. Moreover, all TiN@PCN(Co)-x systems show enhanced light absorption across the visible light region compared to bare PCN(Co), further verifying the effect of TiN LSPR on the light absorption capacity of PCN-222. The presence of TiN does not alter the absorption edges, indicating that the TiN incorporation does not affect the band edge potentials by forming its energy levels in the mid-gaps, ensuring its plasmonic attachment to the PCN-222 system.

The crystal structure of TiN–PCN(Co)-x samples was investigated by X-ray diffraction (XRD), with the resulting patterns shown in Fig. 1C. Characteristic diffraction peaks of PCN-222 are observed at 2θ values of $\sim$4.8°, 7.0° and 9.6°, which align with its previously reported structures.[20] The TiN–PCN systems have the same pattern as bare PCN, demonstrating that they

also share a similar crystal structure. Furthermore, the XRD spectra of TiN@PCN(Co)-x also reveal the presence of TiN crystalline planes (111), (200), and (220) at 2θ values of 36.6°, 42.6°, and 61.8°, respectively, consistent with the reference peaks of TiN reported in the literature.[22] These diffraction peaks provide clear evidence for the successful incorporation of TiN nanoparticles into the PCN structure. Notably, no shifts in the XRD peaks corresponding to PCN and TiN are observed in the composite systems. This indicates that TiN interacts with PCN not at the lattice level but rather through surface attachment, facilitating the metal–semiconductor configuration conducive to plasmonic and Ohmic interactions between the materials.

The structural properties of the obtained materials were further investigated using FT-IR analysis (Fig. 2A). The FT-IR spectra reveal characteristic peaks in the range of 500–700 cm^{-1}, corresponding to the asymmetric vibration of the C=N, N–H, C=C and C–H of the pyrrole ring.[23] The small stretching band observed at 1709 cm^{-1} is related to the C=O bond in the carboxyl group, indicating the coordination between –COOH and Zr atoms.[24] As observed, the nanocomposites displayed a reduced intensity at this peak, indicating the formation of intimate surface bonding between NH$_2$-functionalized TiN and PCN(Co). The Co–N bond is identified by the prominent peak at 1001 cm^{-1}, further confirming the coordination between the Co atoms and the pyrrole rings.[20] For TiN spectra, a broad peak at 1864 cm^{-1} is observed, which could be attributed to the characteristic stretching vibration of TiN. The presence of this peak in all composites, except bare PCN(Co), further verifies the integration of TiN within PCN-222.

The surface area of the bare PCN(Co) and TiN@PCN(Co)-x systems was investigated using the BET N$_2$ adsorption–desorption technique. As shown in Fig. 2B, the sorption curves of PCN(Co) exhibit a type-IV isotherm, suggesting the formation of a mesoporous structure. The bare PCN(Co) demonstrated a high BET surface area of 1355 m^2 g^{-1}, while the TiN@PCN(Co)-5 nanocomposite exhibited a slightly reduced surface area of 1240 m^2 g^{-1}. This minor reduction suggests that the integration of functionalized TiN with PCN induces slight structural modifications due to the chemical bonding of TiN–NH$_2$ and the
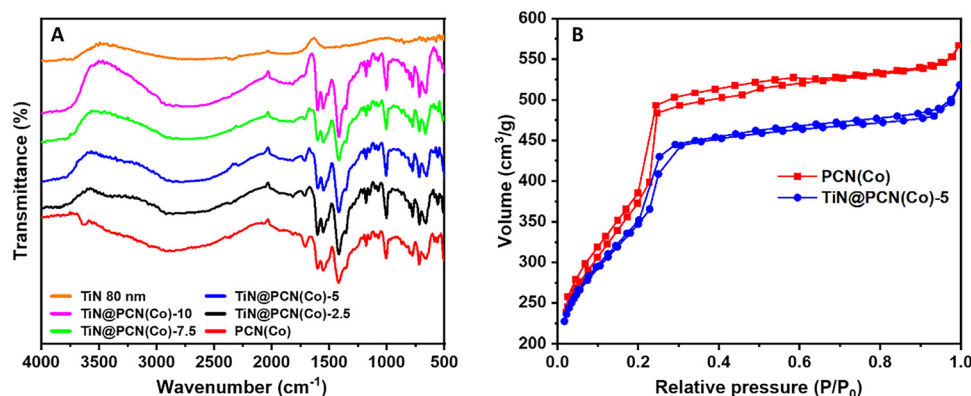

Fig. 2 (A) FT-IR spectra and (B) BET N$_2$ isotherms of PCN(Co) and the TiN@PCN-5 nanocomposite.

16292 | *J. Mater. Chem. C*, 2025, **13**, 16289–16301

This journal is © The Royal Society of Chemistry 2025

host PCN(Co) MOF. Despite this reduction, the interaction between TiN and PCN is expected to enhance charge transfer within the nanocomposite, thereby contributing to improved photocatalytic activity. Additionally, the Barrett–Joyner–Halen (BJH) pore size distribution analysis (Fig. S2, ESI†) reveals a uniform mesopore centered around 2.25 nm for PCN-222(Co) and TiN@PCN-222(Co)-5, consistent with the mesoporous nature of the materials. This porous structure is advantageous for maximizing accessible active sites, facilitating mass transport, which is highly beneficial for CO_2 activation and reaction.

The morphology and microstructure of bare PCN(Co) and TiN@PCN(Co) nanocomposites were further observed using a transmission electron microscope (TEM). As shown in Fig. 3A, both samples exhibit a combination of rod-like and cubic morphologies, with sizes ranging from 1 to 4 μm. The morphological diversity in PCN(Co) is likely influenced by the presence of TiN–NH_2 during synthesis, which affects the deprotonation degree of carboxylic groups in the TCPP ligands. Such an effect alters the coordination environment between Zr_6 clusters and TCPP ligands, leading to variations in structural connectivity and resulting in the formation of both rod- and cube-shaped nanostructures.[25] This morphological variation further confirmed the intimate interaction between TiN–NH_2 and PCN(Co) through amino–carboxyl bonding. In addition, Fig. 3B and C reveal the presence of TiN nanoparticles, ranging in size from 30 to 50 nm, which are uniformly distributed across both morphologies. The intimate contact between TiN nanoparticles and PCN(Co) facilitates efficient charge transfer at the interface, which is crucial for enhancing the photocatalytic performance of the nanocomposite.

Elemental mapping analysis (Fig. 4) was performed to investigate the spatial distribution of the elements in the TiN@PCN(Co) composite. The mapping images confirm the homogeneous distribution of C, N, O, Ni and Co across the selected area, indicating the uniform presence of these elements in the composite matrix. The presence of Ti in well-defined regions confirms the integration of TiN within the PCN-222(Co) matrix. Notably, while C, O, Zr, and Co exhibit uniform distribution, the N signal appears more concentrated in specific areas corresponding to TiN regions. This could be

attributed to the nitrogen-rich nature of TiN, leading to localized intensification of the N signal. To provide a more representative assessment, Fig. S3 (ESI†) presents an additional elemental mapping image, demonstrating a uniform N distribution throughout the TiN@PCN(Co) composite.

The oxidation states and chemical environment of the elements in the bare PCN(Co) and TiN@PCN(Co)-5 system were analyzed using the XPS technique, and the obtained spectra are shown in Fig. 5, with the peaks recalibrated based on the C 1s peak at 284.8 eV. The high-resolution C 1s spectrum of bare PCN(Co) is deconvoluted into three peaks at 284.8, 288.3, and 292.0 eV, corresponding to –C=C– bonds from aromatic rings and adventitious carbon, C–N bonds from pyrrole rings, and carboxylate or carboxylic (–COO) groups, respectively (Fig. 5A).[26] The C 1s spectrum of the TiN@PCN(Co)-5 nanocomposite also exhibits two prominent peaks at 284.8 eV and 288.3 eV, corresponding to the –C=C– and C–N bonds, respectively. These peaks are consistent with those observed in the bare PCN(Co), indicating that the core carbon framework of the metalloporphyrin remains intact upon composite formation. However, a notable shift to higher binding energies is observed in the –COO group. This positive shift in binding energy suggests the formation of chemical interactions between the –COOH groups of PCN(Co) and the –NH_2 functional groups present on the surface of the TiN nanoparticles. Such interactions can lead to electron withdrawal from the carboxylate group, thereby increasing its binding energy. This observation supports the successful integration of TiN nanoparticles into the PCN(Co) structure and indicates strong interfacial interactions that may influence the electronic properties of the composite.

Meanwhile, the XPS spectra of other elements (N, Co, and Zr) of the 2 samples do not show any significant shift in their respective deconvoluted peaks. The N 1s spectra, shown in Fig. 5B, of both materials exhibit 2 deconvoluted peaks at 398.6 and 400.8 eV. The lower binding energy peak, corresponding to N–Co bonds, confirms the strong interaction between cobalt and nitrogen in the metalloporphyrin network,[27] while the peak at 400.8 eV indicates the presence of *N*-pyrrolic bonds in the structure. The Co 2p spectrum, shown in Fig. 5C, displays a prominent peak at 780.8 eV, associated with the Co $2p_{3/2}$ orbital, confirming that cobalt exists in the Co^{2+} oxidation state. This oxidation state is stabilized through interactions with nitrogen atoms in pyrrole rings, ensuring the structural integrity of the composite.[28] In addition, the Zr 3d spectrum (Fig. 5D) shows two peaks at 182.8 and 185.2 eV, assigned to the Zr $3d_{5/2}$ and $3d_{3/2}$ orbitals, respectively, indicating that Zr is present in the +4 oxidation state. This confirms the structural role of Zr_6 clusters in maintaining the stability of the PCN-222 framework.[29] The successful integration of TiN nanoparticles within the composite is confirmed by the Ti 2p spectrum (Fig. 5E), which exhibits four peaks at 459.8, 465.5, 457.3, and 461.9 eV. The two peaks at 459.8 and 457.3 eV are assigned to the N–Ti–O_x bonds, while the peaks at 465.5 and 461.9 eV correspond to Ti–N bonds,[18] confirming strong interfacial interactions between TiN and PCN(Co).

Furthermore, the Si 2p spectrum reveals a peak at 103.2 eV, corresponding to Si–O bonds, providing additional evidence for
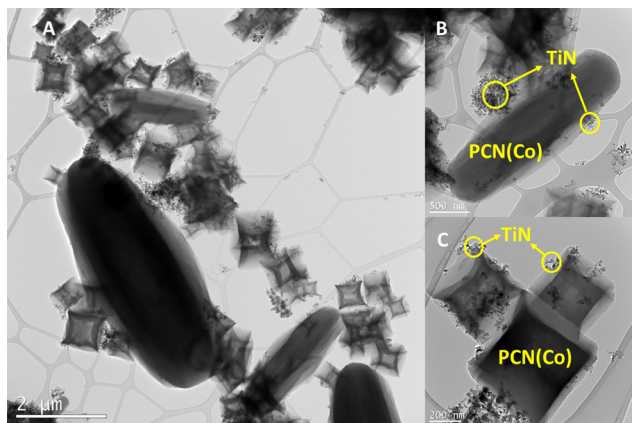

Fig. 3 (A)–(C) TEM images of the TiN@PCN(Co) nanocomposite at different scales.

This journal is © The Royal Society of Chemistry 2025

J. Mater. Chem. C, 2025, **13**, 16289–16301 | **16293**
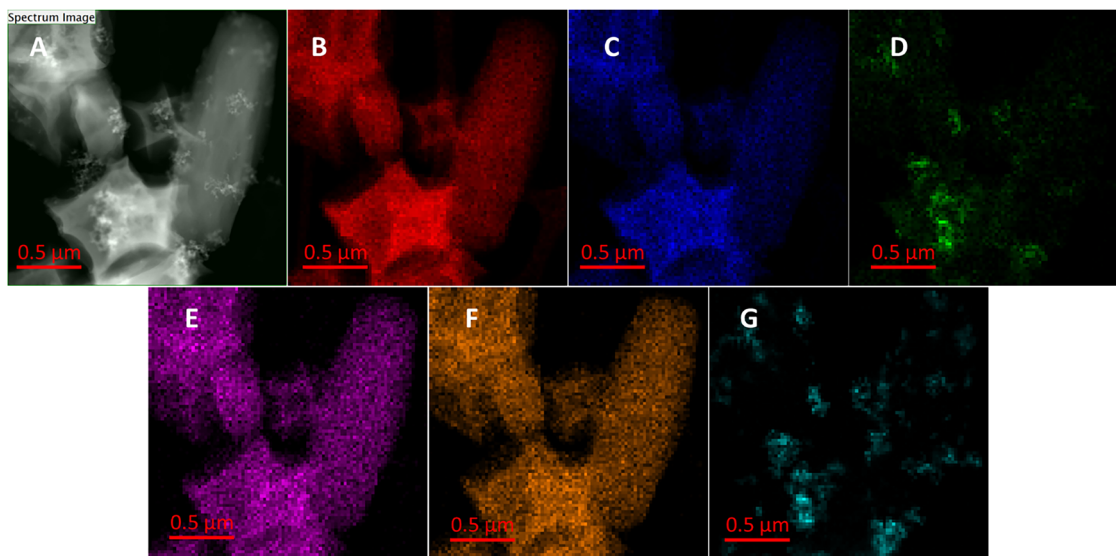
Fig. 4 The EDS elemental mapping images of various elements present in the TiN@PCN(Co)-5 nanocomposite: (A) full area image, (B) C K signal, (C) O K signal, (D) N K signal, (E) Co K signal, (F) Zr K signal, and (G) Ti K signal.

the successful surface functionalization of TiN with $-NH_2$ groups through the slow hydrolysis of APTES. The formation of N–Ti–O–Si bonds further supports the enhanced compatibility and interfacial charge transfer between TiN and the PCN-222(Co) framework. These findings collectively validate the structural and electronic interactions within the TiN@PCN(Co)-5 composite, demonstrating that the integration of TiN nanoparticles with the cobalt-metalated zirconium-metalloporphyrin not only maintains the integrity of the framework but also enhances charge transfer pathways and active sites in the composite system.

The photocatalytic CO_2 reduction under solar light irradiation was performed to evaluate the efficiency of the developed materials. The reaction was conducted in a $MeCN:H_2O:TEOA$ mixed solvent, where CO was identified as the primary reduction product. Firstly, the ratio of the three solvents was investigated to optimize the reaction conditions (Fig. S5, ESI†). It was found that the mixed solvent $MeCN:H_2O:TEOA$ in a 3:1:1 ratio displayed the highest CO production rate. Furthermore, the role of each component in the mixed solvent was confirmed in this control experiment. In the absence of TEOA, the photocatalytic performance is negligible, confirming the necessity of TEOA as a sacrificial agent. Without TEOA, the available electrons for CO_2 reduction are insufficient due to the recombination effect on the photocatalyst. In addition, when water is excluded from the system, the CO production rate is observed to be about 244.7 $\mu mol\ g^{-1}\ h^{-1}$, while the H_2 production rate is about 62.3 $\mu mol\ g^{-1}\ h^{-1}$. The absence of H_2O in the photocatalytic CO_2 reduction system can significantly hinder the overall performance, as it serves as a proton source for the reduction process. Without adequate proton supply, the conversion efficiency of CO_2 to CO is significantly suppressed. Overall, MeCN enhances the solubility of CO_2, while water supplies protons that promote the reaction pathway for CO

formation. In addition, TEOA serves as a hole scavenger, effectively promoting charge-carrier separation and minimizing charge recombination.

In this system, the photosensitizer $[Ru(bpy)_3]Cl_2$ plays a crucial role in driving photochemical reactions. As shown in Fig. 6A, neither bare PCN(Co) nor the TiN@PCN-5 nanocomposite exhibited detectable CO_2 reduction activity in the absence of a photosensitizer, indicating that the LSPR effect of TiN alone does not significantly enhance the photocatalytic activity of PCN-222. However, upon the introduction of the $[Ru(bpy)_3]^{2+}$ photosensitizer as an electron donor, a substantial increase in CO and H_2 production was observed across all samples, including both bare PCN(Co) and TiN–PCN(Co). Specifically, bare PCN(Co) achieved CO and H_2 production rates of $\sim$99.31 and 14.9 $\mu mol\ g^{-1}\ h^{-1}$, respectively. In contrast, TiN@PCN(Co)-5 exhibited a significantly enhanced CO production rate of 627.42 $\mu mol\ g^{-1}\ h^{-1}$, while maintaining a comparable H_2 evolution rate of 267.56 $\mu mol\ g^{-1}\ h^{-1}$. This pronounced enhancement highlights the crucial role of $[Ru(bpy)_3]^{2+}$ as an electron donor and the single-atom Co sites as active co-catalysts for CO_2 reduction to CO. To further explore the influence of TiN concentration on photocatalytic performance, a series of TiN@PCN(Co)-x samples with varying TiN contents were tested. The results revealed a strong correlation between TiN loading and CO production rates, where TiN@PCN(Co)-2.5, TiN@PCN(Co)-5, TiN@PCN(Co)-7.5, and TiN@PCN(Co)-10 exhibited CO evolution rates of 550.95, 627.42, 409.80, and 352.10 $\mu mol\ g^{-1}\ h^{-1}$, respectively. Among these, TiN@PCN(Co)-5 demonstrated the highest CO production, indicating that an optimal TiN concentration facilitates effective charge transfer while preventing excessive nanoparticle aggregation, which could otherwise limit photocatalytic activity.

These findings suggest that enhanced visible-light absorption due to plasmonic TiN incorporation does not directly contribute to the photocatalytic activity of TiN–PCN(Co). However, in the
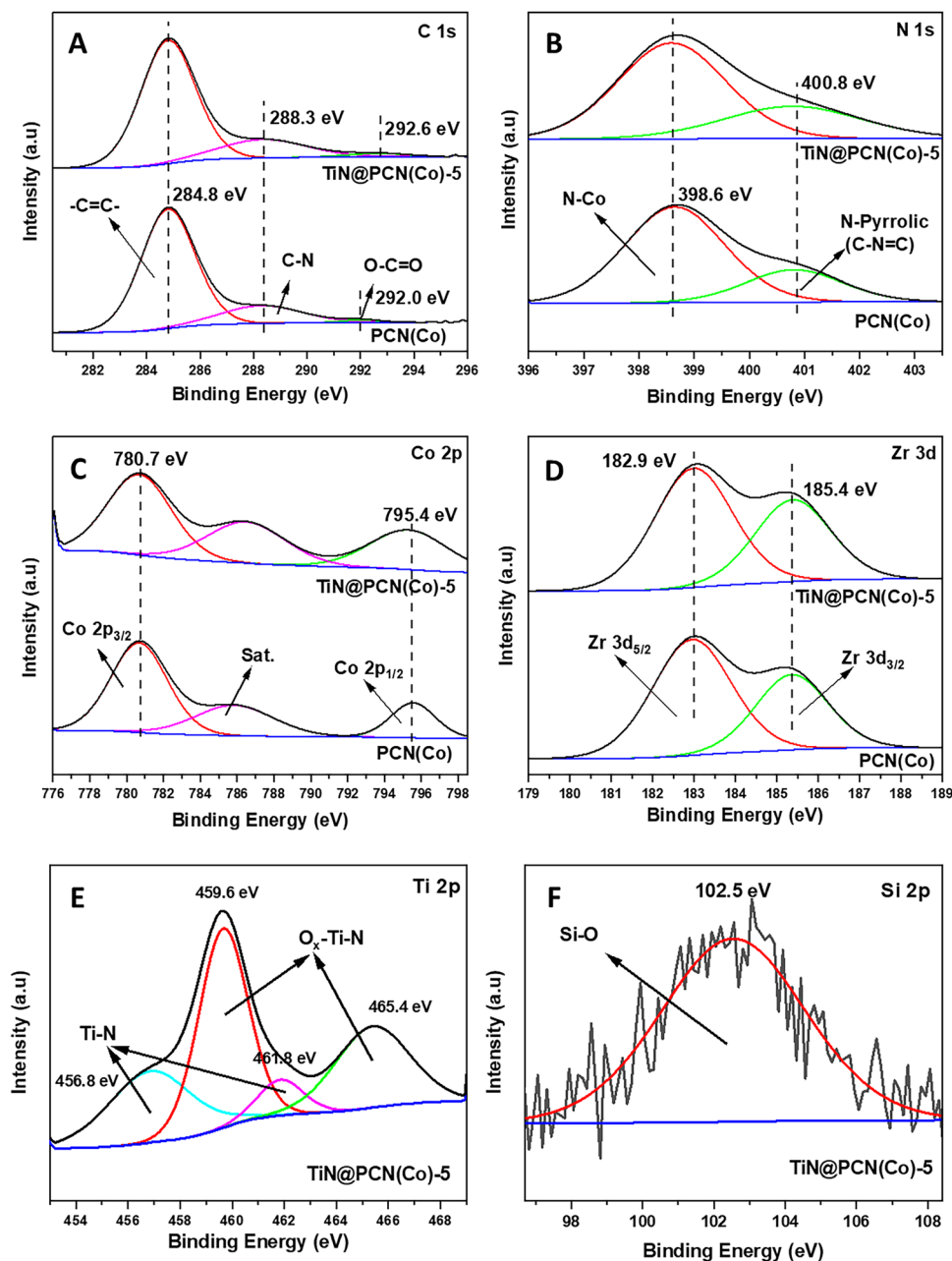
16294 | *J. Mater. Chem. C*, 2025, **13**, 16289–16301

This journal is © The Royal Society of Chemistry 2025

Fig. 5 XPS spectra of bare PCN(Co) and the TiN@PCN(Co)-5 nanocomposite: (A) C 1s, (B) N 1s, (C) Co 2p, (D) Zr 3d, (E) Ti 2p, and (F) Si 2p regions.

presence of the $[Ru(bpy)_3]^{2+}$ photosensitizer, TiN functions as an efficient electron transfer bridge, facilitating electron transport from the photosensitizer to the single-atom Co sites in PCN-222. This role is further substantiated by the significantly higher CO production rates observed in TiN@PCN(Co) nanocomposites compared to bare PCN(Co), confirming the critical function of TiN in promoting efficient charge transfer and enhancing CO_2 reduction efficiency.

The significance of the intimate bonding between TiN–NH$_2$ and PCN(Co) was further validated through comparative experiments (Fig. 6C). Under identical reaction conditions, the functionalized TiN (TiN@PCN(Co)-5) exhibited superior photocatalytic performance compared to the non-functionalized TiN (TiN@PCN-

(Co)-5(nf)), demonstrating that the covalent bonding between TiN nanoparticles and PCN(Co) plays a crucial role in facilitating efficient electron transfer. This result underscores the necessity of chemical interactions between TiN–NH$_2$ and PCN(Co) in enhancing charge transport across the composite system.

The stability of TiN@PCN(Co)-5 was assessed through five consecutive 4-hour photocatalytic cycles under the same reaction conditions. As shown in Fig. 6D, the composite retained its photocatalytic activity over multiple cycles, exhibiting consistent CO production with minimal decline in efficiency. This stability confirms the robust interaction between TiN and PCN(Co), ensuring sustained electron transfer and long-term catalytic performance. Additionally, structural analyses before
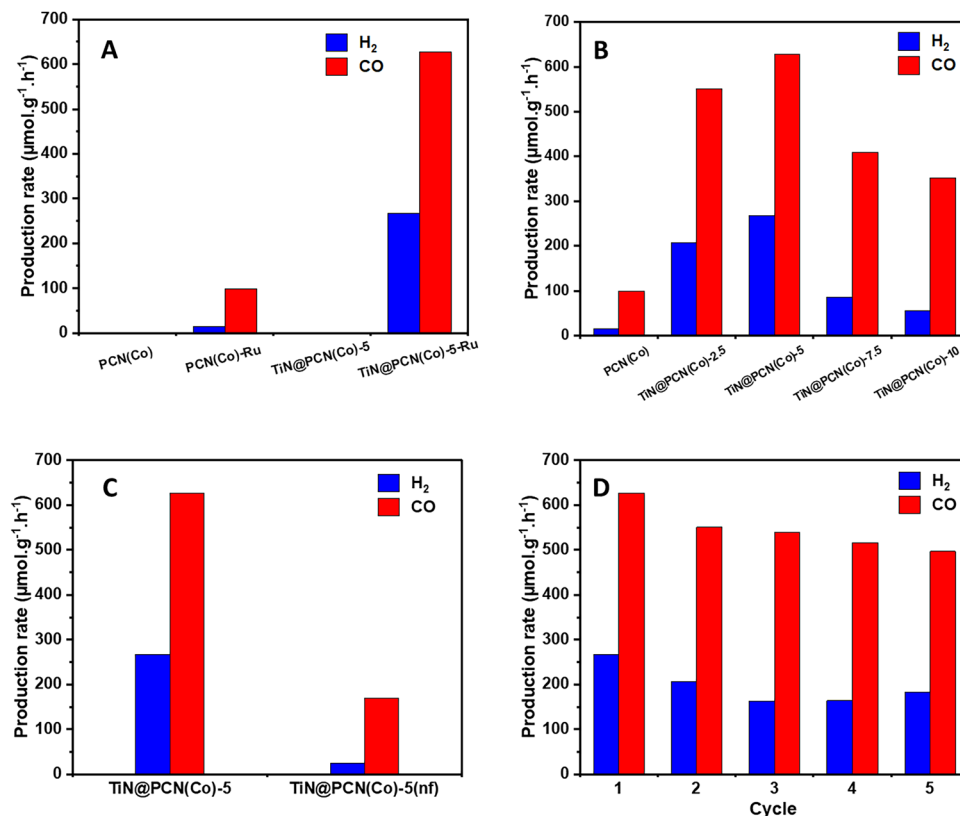
This journal is © The Royal Society of Chemistry 2025

J. Mater. Chem. C, 2025, **13**, 16289–16301 | **16295**

Fig. 6 (A) The comparison of photocatalytic activity between PCN(Co) and the TiN@PCN(Co)-5 nanocomposite with and without the photosensitizer $[Ru(bpy)_3]^{2+}$, (B) the photocatalytic performance of PCN(Co) and TiN@PCN(Co)-x under solar light irradiation in the presence of the photosensitizer, (C) the comparison of photocatalytic activity between TiN@PCN(Co)-5 and the reference sample, and (D) the stability test of TiN@PCN(Co)-5 under five cycles.

and after the stability tests were performed using FT-IR and XRD techniques (Fig. S6, ESI†). The results showed negligible changes in the characteristic peaks of TiN@PCN(Co)-5, further confirming the stability of the material.[30,31]

To further validate the charge transfer properties and the enhanced photocatalytic activity of the TiN@PCN(Co)-5 composite, a series of photoelectrochemical characterization tests were conducted, including linear sweep voltammetry (LSV), transient photocurrent measurements, electrochemical impedance spectroscopy (EIS), and the Mott–Schottky analysis. The steady-state photocurrent response was recorded over 10-second on–off cycles for both PCN(Co) and TiN@PCN(Co)-5, as shown in Fig. 7A. Upon light irradiation, all TiN@PCN(Co)-x nanocomposites exhibited a significantly higher photocurrent density compared to PCN(Co), indicating a more efficient charge separation and transport. When the light was ON, the photocurrent density values of TiN@PCN(Co)-2.5 and TiN@PCN(Co)-5 reached up to ~ 0.15 μA cm^{-2}, while upon switching the light OFF, the density dropped sharply to 0.05 μA cm^{-2}. In contrast, the photocurrent density values of TiN@PCN(Co)-7.5 and TiN@PCN(Co)-10 were considerably lower, which could be attributed to the high amount of TiN NPs that could hinder the charge transfer efficiency. This observation is further supported by electrochemical impedance spectroscopy (EIS). EIS measurements were performed to investigate the charge transfer

behavior at the electrode and electrolyte interface, and the results and the simulated equivalent circuit model are shown in Fig. 7B. The Nyquist plots were fitted using Z-view software, and the used circuit model was $R_s(R_{ct}Q)$, including solution resistance (R_s), charge transfer resistance at the interface electrode/electrolyte (R_{ct}), and the constant phase element (Q). All circuit parameters are listed in Table S1 (ESI†). As shown in Fig. 7B, all TiN@PCN(Co)-x samples exhibit smaller semicircular arcs compared to PCN(Co), signifying a lower charge transfer resistance due to the integration of TiN nanoparticles within the MOF structure. Notably, TiN@PCN(Co)-5 displays a lower R_{ct} value compared to the other nanocomposites, indicating the optimized amount of TiN promoting a more efficient electron transport pathway, thereby enhancing the overall photocatalytic activity of the TiN@PCN(Co)-5 composite.

Photoluminescence (PL) spectroscopy was employed to evaluate the trapping and separation efficiency of photogenerated electron–hole pairs in PCN(Co) and TiN@PCN(Co)-x composites. The PL spectra of bare PCN(Co) and TiN@PCN(Co)-5, excited at 600 nm, are shown in Fig. 7C. The emission peaks, concentrated in the range of 800–860 nm, correspond to the recombination of photoinduced electron–hole pairs. Compared to bare PCN(Co), the TiN@PCN(Co)-5 composite exhibits a significantly lower PL intensity, indicating a reduced electron–hole recombination rate. This effect is further enhanced
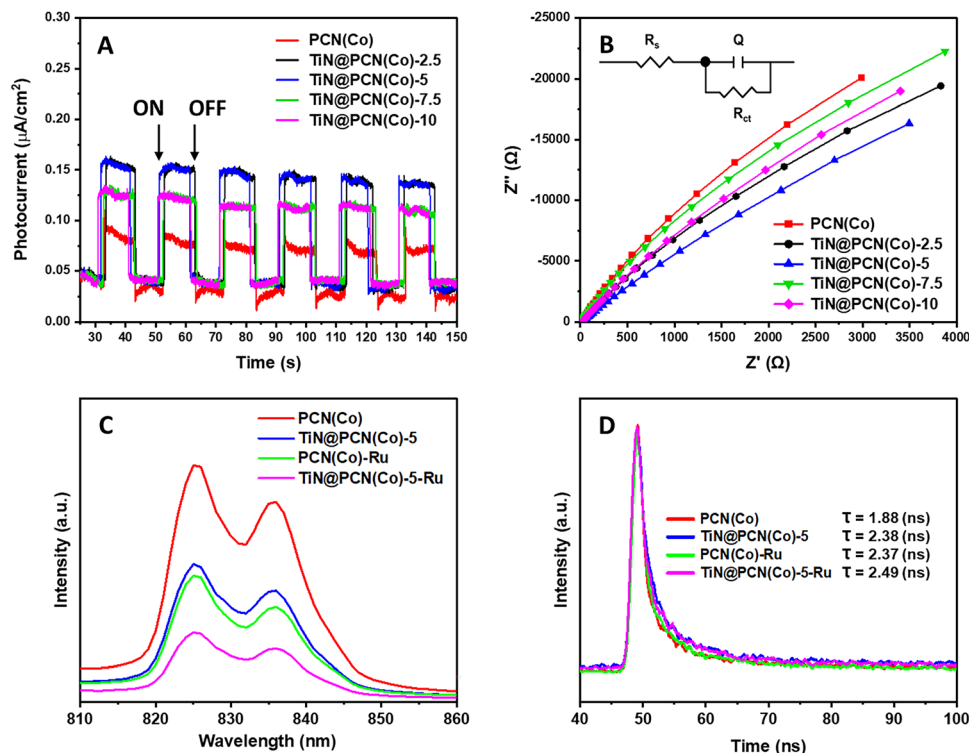
Fig. 7 (A) The photocurrent density *versus* time profiles, (B) Nyquist plots of PCN(Co) and TiN@PCN(Co)-*x* nanocomposites, (C) steady-state photoluminescence, and (D) time-resolved photoluminescence of samples with (PCN(Co) and the TiN@PCN(Co)-5 nanocomposite) and without the photosensitizer [Ru(bpy)$_3$]Cl$_2$·6H$_2$O (PCN(Co)-Ru and TiN@PCN(Co)-5-Ru).

in the presence of the [Ru(bpy)$_3$]$^{2+}$ photosensitizer, which facilitates charge separation and further suppresses recombination, leading to an even lower PL intensity compared to both bare PCN(Co) and TiN@PCN(Co)-5. A similar trend is observed across all TiN@PCN(Co)-*x* composites, as shown in Fig. S7 (ESI†). These findings are corroborated by time-resolved photoluminescence (TRPL) decay spectra (Fig. 7D), whose emission decay curves are fitted using triexponential decay kinetics (Table S2, ESI†). The calculated results reveal that the average lifetime of excited carriers in TiN@PCN(Co)-5 (∼2.38 ns) is significantly longer than that in bare PCN(Co) (∼1.88 ns). Moreover, the presence of [Ru(bpy)$_3$]$^{2+}$ further extends the carrier lifetime, as confirmed by the longer decay time in all photosensitizer-containing samples compared to their non-photosensitized counterparts.

These results collectively demonstrate that the integration of NH$_2$-functionalized TiN and the [Ru(bpy)$_3$]$^{2+}$ photosensitizer significantly enhances charge carrier separation, suppresses recombination, and extends the lifetime of excited carriers. Consequently, this prolonged charge retention facilitates more efficient redox reactions during the photocatalytic process, ultimately improving overall photocatalytic performance.

To elucidate the reaction pathway of photocatalytic CO$_2$ reduction, the band gap energy and flat-band potential of PCN(Co) and TiN@PCN(Co)-5 were investigated. The band gap energies of bare PCN(Co) and TiN@PCN(Co)-5 were determined by Tauc plot fitting (Fig. 8A), yielding values of ∼2.54 eV and 2.41 eV, respectively. The observed band gap narrowing in TiN@PCN(Co)-5 suggests that the formation of chemical bonds

between TiN–NH$_2$ and PCN(Co) enhances light absorption, likely due to improved electronic coupling between the components. Furthermore, the flat-band potential (E_{fb}) of the systems was determined *via* Mott–Schottky analysis, revealing a positive slope in the plot, which confirms the n-type semiconductor nature of the PCN-222 framework, meaning that their respective CB band edges are about 0.1 V more negative than the flat-band potential (E_{fb}).[32] As shown in Fig. 8B and C, the E_{fb} values of PCN(Co) and TiN@PCN(Co)-5 were measured at −1.02 and −1.11 V (*vs.* Ag/AgCl), equivalent to −0.82 and −0.91 V (*vs.* NHE), respectively. Based on these values, the CB potentials were estimated to be approximately −0.92 and −1.01 V (*vs.* NHE), respectively. Given that the indirect band gap of PCN(Co) and TiN@PCN(Co)-5 is 2.54 and 2.41 eV, the valence band (VB) potential was calculated as 1.62 and 1.4 V (*vs.* NHE), respectively. These results indicate that both PCN(Co) and TiN@PCN(Co)-5 possess a conduction band potential more negative than the CO$_2$/CO redox potential (−0.53 V *vs.* NHE), making the CO$_2$-to-CO conversion thermodynamically favorable under visible light irradiation (Fig. 8D).

Furthermore, the redox potential of the [Ru(bpy)$_3$]$^{2+}$ photosensitizer is −1.31 V (*vs.* NHE), which is more negative than the CB potential of TiN@PCN(Co)-5. This ensures that electron transfer from [Ru(bpy)$_3$]$^{2+}$ to the CB of TiN@PCN(Co)-5 is also thermodynamically feasible, further enhancing charge separation and driving CO$_2$ reduction efficiently.

Based on comprehensive investigations using XRD, FT-IR spectroscopy, UV-vis spectroscopy, TEM, photoelectrochemical

This journal is © The Royal Society of Chemistry 2025

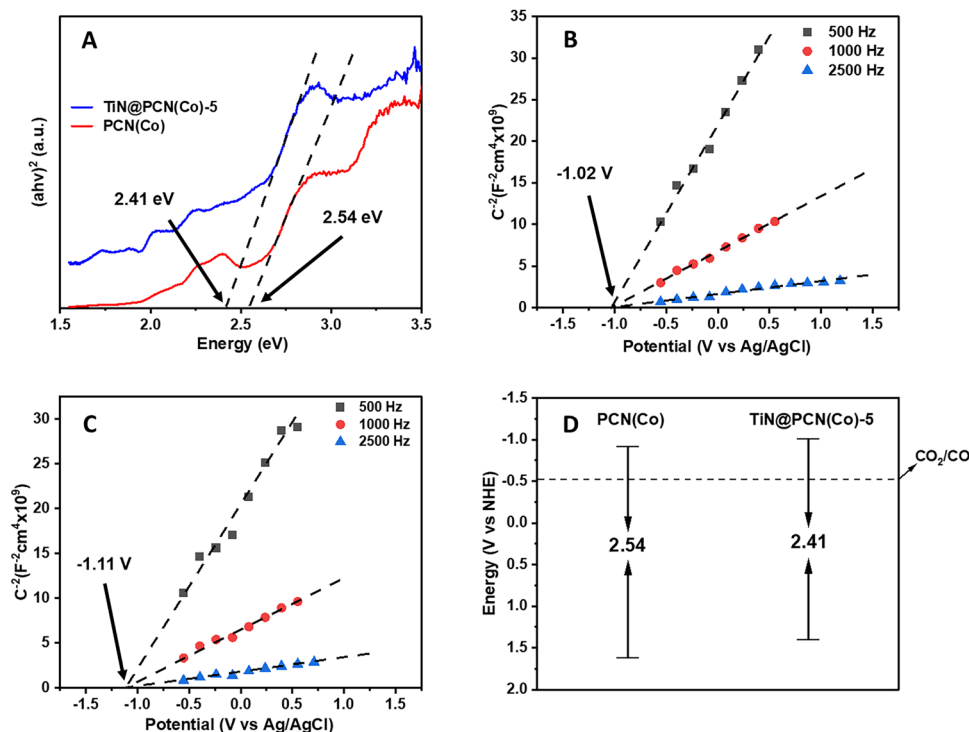*J. Mater. Chem. C*, 2025, **13**, 16289–16301 | **16297**

Fig. 8 (A) Tauc's plots for band gap energy estimation, Mott−Schottky analysis of (B) PCN(Co) and (C) the TiN@PCN(Co)-5 nanocomposite, and (D) band structure positions for PCN(Co) and TiN@PCN(Co)-5.

measurements, and photoluminescence analysis, a plausible CO_2 reduction mechanism is proposed, as illustrated in Fig. 9. In this photocatalytic system, TiN nanoparticles serve as a charge transfer bridge, facilitating electron migration between

Fig. 9 Schematic illustration of the charge transfer mechanism for CO_2 photoreduction over the TiN@PCN(Co)-5 nanocomposite with TEOA as the sacrificial agent.

the $[Ru(bpy)_3]^{2+}$ photosensitizer and the PCN(Co) MOF. Meanwhile, TEOA functions as a sacrificial agent, effectively scavenging photogenerated holes to suppress recombination.

Under visible-light irradiation, $[Ru(bpy)_3]Cl_2$ absorbs photon energy and transitions to its excited state $[Ru(bpy)_3]^{2+*}$. This leads to the generation of electron–hole pairs, with electrons being injected into both the CB of TiN (*via* its Fermi level) and the LUMO of PCN-222, producing $[Ru(bpy)_3]^{3+}$. The oxidized photosensitizer $[Ru(bpy)_3]^{3+}$ is subsequently reduced back to $[Ru(bpy)_3]^{2+}$ by TEOA, ensuring its continuous participation in multiple excitation cycles. Furthermore, TiN nanoparticles generate "hot electrons" through localized surface plasmon resonance (LSPR) effects under light irradiation. These high-energy electrons, along with those from the photosensitizer, migrate to the CB of PCN(Co) *via* amino–carboxyl bonds within the nanocomposite. The presence of chemical bonding (rather than mere physical interactions) significantly enhances charge transfer efficiency compared to bare PCN(Co). As a result, PCN(Co) accumulates electrons from multiple sources such as TiN, the photosensitizer, and its own photogenerated carriers, substantially boosting the electron density at its CB. These electrons are then channeled toward the single-Co active sites of the photocatalyst, driving CO_2 reduction to CO. Simultaneously, the photogenerated holes in the VB of $[Ru(bpy)_3]^{2+}$, TiN, and PCN(Co) are efficiently consumed by TEOA, suppressing charge recombination and thereby enhancing the overall photocatalytic efficiency.

To gain deeper insight into the reaction mechanism of CO_2 photoreduction at the cobalt active site, we propose a plausible
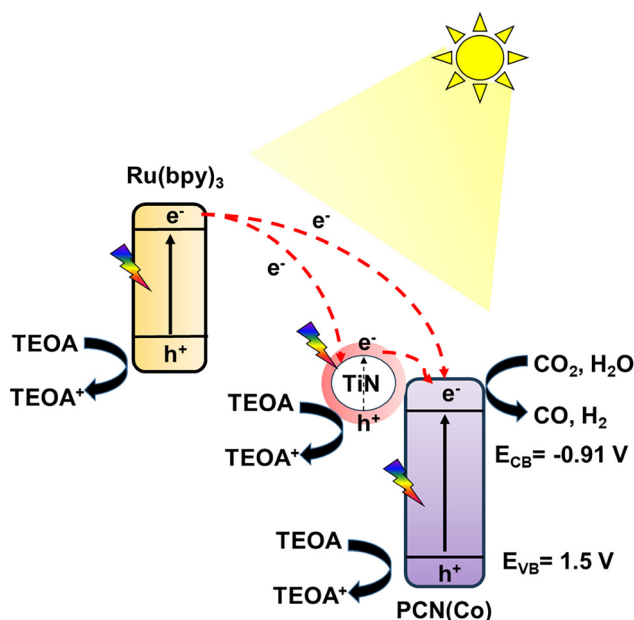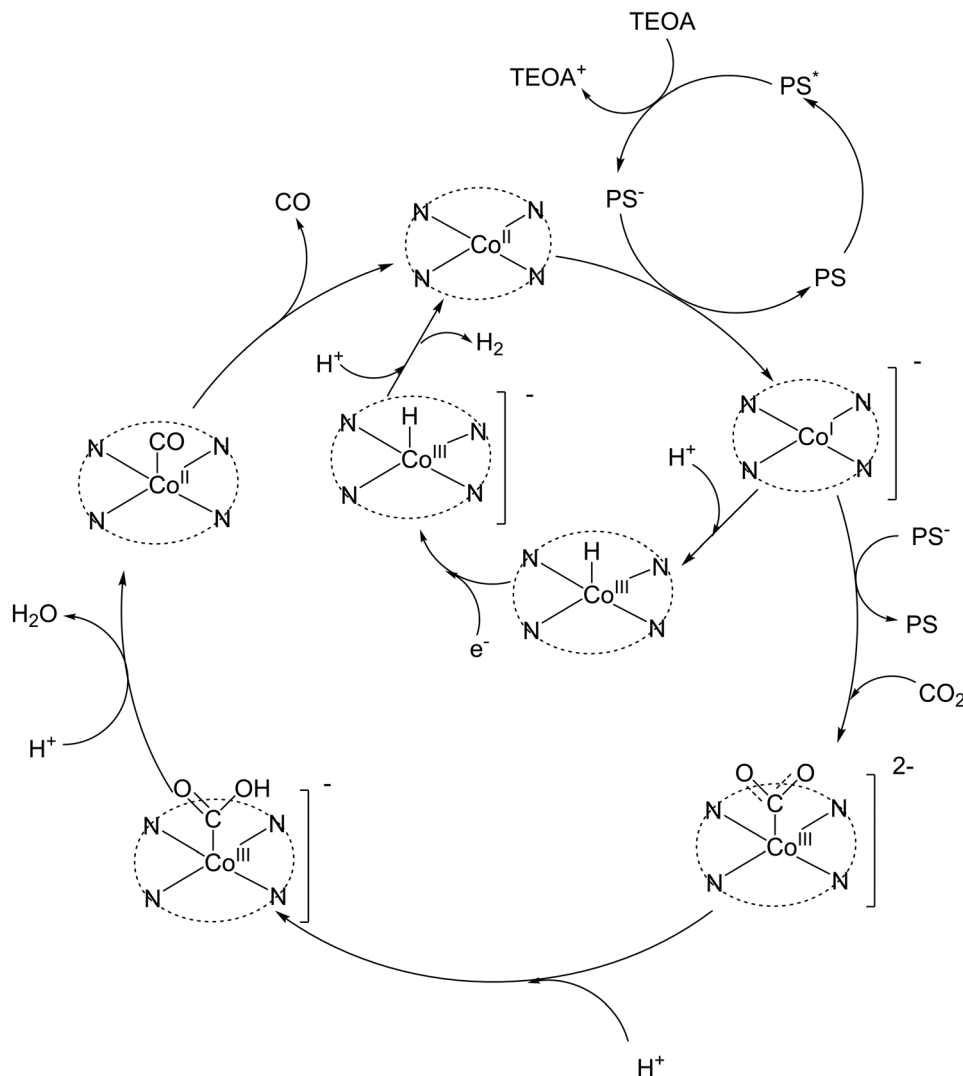
16298 | *J. Mater. Chem. C*, 2025, **13**, 16289–16301

This journal is © The Royal Society of Chemistry 2025

Scheme 1 Proposed reaction scheme for the photocatalytic CO_2-to-CO conversion in the $Ru(bpy)_3]^{2+}$/TEOA/TiN@PCN(Co) systems.

photocatalytic cycle based on previous literature.[33,34] This mechanism, as shown in Scheme 1, involves a cobalt-porphyrin-based catalyst undergoing a series of redox transformations that play a crucial role in facilitating the CO_2 reduction process. Initially, upon light absorption, the photosensitizer (PS) $[Ru(bpy)_3]^{2+}$ enters an excited state and transfers an electron to the cobalt center, reducing Co^{II} to the catalytically active $(Co^I)^-$ species. This $(Co^I)^-$ intermediate is further reduced by PS for CO_2 activation, forming a Co^{III}–CO_2 species. A series of protonation processes of this intermediate lead to the formation of a Co^{II}–CO species, which releases CO as the primary product, thereby regenerating the Co^{II} catalyst. In parallel, H_2 is also generated as a side product through proton reduction pathways.

Overall, the ability of the Co center to cycle between Co^{III}/ Co^{II}/Co^I oxidation states is crucial for efficient CO_2 photoreduction. The Co^I species serve as the key active intermediate for CO_2 activation, while the higher oxidation states play roles in

electron transfer and catalyst regeneration at the end of each catalytic cycle.

4. Conclusion

In this study, a facile strategy for synthesizing chemically bonded plasmonic titanium nitride (TiN)-incorporated PCN-222(Co) with enhanced photocatalytic performance has been successfully demonstrated. The remarkable improvement in photocatalytic activity is attributed to TiN and its strong chemical interaction with PCN(Co), which significantly facilitates electron transfer, as confirmed by comprehensive characterization and experimental analyses. This study provides new insights into the role of TiN in MOF-based semiconductors, demonstrating that, even with minimal plasmonic resonance, the covalent bonding between TiN and PCN(Co) serves as an effective strategy for improving photocatalytic efficiency.

These findings open new avenues for the integration of TiN into diverse photocatalytic systems, paving the way for future advancements in MOF-based hybrid materials for sustainable energy applications.

Conflicts of interest

There are no conflicts to declare.

Data availability

The data supporting this article have been included as part of the ESI.†

Acknowledgements

References

1 S. Overa, B. H. Ko, Y. Zhao and F. Jiao, Electrochemical approaches for CO2 conversion to chemicals: a journey toward practical applications, *Acc. Chem. Res.*, 2022, **55**(5), 638–648.

2 S. Roy, A. Cherevotan and S. C. Peter, Thermochemical CO2 hydrogenation to single carbon products: scientific and technological challenges, *ACS Energy Lett.*, 2018, **3**(8), 1938–1966.

3 R. Gupta, A. Mishra, Y. Thirupathaiah and A. K. Chandel, Biochemical conversion of CO2 in fuels and chemicals: status, innovation, and industrial aspects, *Biomass Convers. Biorefin.*, 2024, **14**(3), 3007–3030.

4 Z. Fu, Q. Yang, Z. Liu, F. Chen, F. Yao, T. Xie, Y. Zhong, D. Wang, J. Li and X. Li, Photocatalytic conversion of carbon dioxide: From products to design the catalysts, *J. CO2 Util.*, 2019, **34**, 63–73.

5 Y. Wang, E. Chen and J. Tang, Insight on reaction pathways of photocatalytic CO2 conversion, *ACS Catal.*, 2022, **12**(12), 7300–7316.

6 U. Ulmer, T. Dingle, P. N. Duchesne, R. H. Morris, A. Tavasoli, T. Wood and G. A. Ozin, Fundamentals and applications of photocatalytic CO2 methanation, *Nat. Commun.*, 2019, **10**(1), 3169.

7 Z. Yuan, X. Zhu, X. Gao, C. An, Z. Wang, C. Zuo, D. D. Dionysiou, H. He and Z. Jiang, Enhancing photocatalytic CO2 reduction with TiO2-based materials: Strategies, mechanisms, challenges, and perspectives, *Environ. Sci. Ecotechnol.*, 2023, 100368.

8 J. A. Torres, A. E. Nogueira, G. T. da Silva and C. Ribeiro, The Effect of SnO2 Surface Properties on CO2 Photoreduction to Higher Hydrocarbons, *ChemCatChem*, 2023, **15**(6), e202201534.

9 H.-C. Hsu, I. Shown, H.-Y. Wei, Y.-C. Chang, H.-Y. Du, Y.-G. Lin, C.-A. Tseng, C.-H. Wang, L.-C. Chen and Y.-C. Lin, Graphene oxide as a promising photocatalyst for CO2 to methanol conversion, *Nanoscale*, 2013, **5**(1), 262–268.

10 U. Ghosh, A. Majumdar and A. Pal, Photocatalytic CO2 reduction over g-C3N4 based heterostructures: Recent progress and prospects, *J. Environ. Chem. Eng.*, 2021, **9**(1), 104631.

11 S. Navalón, A. Dhakshinamoorthy, M. Álvaro, B. Ferrer and H. García, Metal–organic frameworks as photocatalysts for solar-driven overall water splitting, *Chem. Rev.*, 2022, **123**(1), 445–490.

12 Q. Wang, Q. Gao, A. M. Al-Enizi, A. Nafady and S. Ma, Recent advances in MOF-based photocatalysis: environmental remediation under visible light, *Inorg. Chem. Front.*, 2020, **7**(2), 300–339.

13 Q. Su, Q. Guo, H. Wang, M. Liu and C. Zuo, Research progress of MOF-based materials in the photocatalytic CO2 reduction, *Carbon Resour. Convers.*, 2023, 100211.

14 T.-A. Quach, M.-K. Duong, S. Mohan and T.-O. Do, Cobalt-Atom Active Sites Grafted UiO-66-NH2 via EDTA for the Enhanced Production of Syngas in CO2 Photoreduction, *ACS Appl. Energy Mater.*, 2024, **7**, 8797–8806.

15 P. Wang, X. Ba, X. Zhang, H. Gao, M. Han, Z. Zhao, X. Chen, L. Wang, X. Diao and G. Wang, Direct Z-scheme heterojunction of PCN-222/CsPbBr3 for boosting photocatalytic CO2 reduction to HCOOH, *Chem. Eng. J.*, 2023, **457**, 141248.

16 E. Pena, J. Becerra, V. N. Gopalakrishnan and T.-O. Do, Facile one-pot synthesis of plasmonic gold nanoparticles decorated porphyrin-metal organic framework for photocatalytic hydrogen evolution, *Mol. Catal.*, 2023, **548**, 113470.

17 H. Jia, D. Ma, S. Zhong, L. Li, L. Li, L. Xu and B. Li, Boosting photocatalytic activity under visible-light by creation of PCN-222/g-C3N4 heterojunctions, *Chem. Eng. J.*, 2019, **368**, 165–174.

18 D.-T. Nguyen and T.-O. Do, Plasmonic Titanium Nitride/g-C3N4 with Inherent Interface Facilitates Photocatalytic CO2 Reduction, *ACS Appl. Energy Mater.*, 2022, **6**(1), 89–98.

19 D. Feng, Z. Y. Gu, J. R. Li, H. L. Jiang, Z. Wei and H. C. Zhou, Zirconium-metalloporphyrin PCN-222: mesoporous metal–organic frameworks with ultrahigh stability as biomimetic catalysts, *Angew. Chem., Int. Ed.*, 2012, **51**(41), 10307.

20 S. Carrasco; A. Sanz-Marco; B. Martín-Matute, *Fast and robust synthesis of metalated PCN-222 and their catalytic performance in cycloaddition reactions with CO2*. Organometallics, 2019, **38**(18), 3429–3435.

21 R. A. Karaballi, G. Humagain, B. R. Fleischman and M. Dasog, Synthesis of Plasmonic Group-4 Nitride Nanocrystals by Solid-State Metathesis, *Angew. Chem.*, 2019, **131**(10), 3179–3182.

22 X. Li, H. Xu and W. Yan, Fabrication and characterization of a PbO2-TiN composite electrode by co-deposition method, *J. Electrochem. Soc.*, 2016, **163**(10), D592.

23 A. Zuliani, M. C. Castillejos and N. Khiar, Continuous flow synthesis of PCN-222 (MOF-545) with controlled size and morphology: a sustainable approach for efficient production, *Green Chem.*, 2023, **25**(24), 10596–10610.

16300 | *J. Mater. Chem. C*, 2025, **13**, 16289–16301

This journal is © The Royal Society of Chemistry 2025

24 J. Jin, Highly stable and efficient visible-light-driven carbon dioxide reduction by zirconium–metalloporphyrin PCN-222 via dual catalytic routes. Reaction Kinetics, *Mech. Catal.*, 2020, **131**(1), 397–408.

25 J. Yang, X. Chen, Y. Li, Q. Zhuang, P. Liu and J. Gu, Zr-based MOFs shielded with phospholipid bilayers: improved biostability and cell uptake for biological applications, *Chem. Mater.*, 2017, **29**(10), 4580–4589.

26 S. Nazri, M. Khajeh, A. R. Oveisi, R. Luque, E. Rodriguez-Castellon and M. Ghaffari-Moghaddam, Thiol-functionalized PCN-222 MOF for fast and selective extraction of gold ions from aqueous media, *Sep. Purif. Technol.*, 2021, **259**, 118197.

27 M. Aghayan, A. Mahmoudi, K. Nazari, S. Dehghanpour, S. Sohrabi, M. R. Sazegar, N. Mohammadian-Tabrizi and I. I. I. Fe, porphyrin metal–organic framework as an artificial enzyme mimics and its application in biosensing of glucose and H2O2, *J. Porous Mater.*, 2019, **26**, 1507–1521.

28 C. Strydom and H. Strydom, X-ray photoelectron spectroscopy studies of some cobalt(II) nitrate complexes, *Inorg. Chim. Acta*, 1989, **159**(2), 191–195.

29 H. Xing, S. Teng, Z. Xing, L. Bi, Q. Bu, T. Xie and W. Yang, Effect of Pt cocatalyst on visible light driven hydrogen evolution of anthracene-based zirconium metal-organic framework, *Appl. Surf. Sci.*, 2020, **532**, 147000.

30 B. Su, S. Wang, W. Xing, K. Liu, S.-F. Hung, X. Chen, Y. Fang, G. Zhang, H. Zhang and X. Wang, Synergistic Ru Species on Poly (heptazine imide) Enabling Efficient Photocatalytic CO2 reduction with H2O Beyond 800 nm, *Angew. Chem., Int. Ed.*, 2025, e202505453.

31 G. Zhang, G. Li, T. Heil, S. Zafeiratos, F. Lai, A. Savateev, M. Antonietti and X. Wang, Tailoring the grain boundary chemistry of polymeric carbon nitride for enhanced solar hydrogen production and CO2 reduction, *Angew. Chem., Int. Ed.*, 2019, **58**(11), 3433–3437.

32 E. Koshevoy, E. Gribov, D. Polskikh, M. Lyulyukin, M. Solovyeva, S. Cherepanova, D. Kozlov and D. Selishchev, Photoelectrochemical methods for the determination of the flat-band potential in semiconducting photocatalysts: A comparison study, *Langmuir*, 2023, **39**(38), 13466–13480.

33 A. Call, M. Cibian, K. Yamamoto, T. Nakazono, K. Yamauchi and K. Sakai, Highly efficient and selective photocatalytic CO2 reduction to CO in water by a cobalt porphyrin molecular catalyst, *ACS Catal.*, 2019, **9**(6), 4867–4874.

34 Y. C. Cao, L. L. Shi, M. Li, B. You and R. Z. Liao, Deciphering the selectivity of the electrochemical CO2 reduction to CO by a cobalt porphyrin catalyst in neutral aqueous solution: insights from DFT calculations, *ChemistryOpen*, 2023, **12**(2), e202200254.

This journal is © The Royal Society of Chemistry 2025

J. Mater. Chem. C, 2025, **13**, 16289–16301 | **16301**